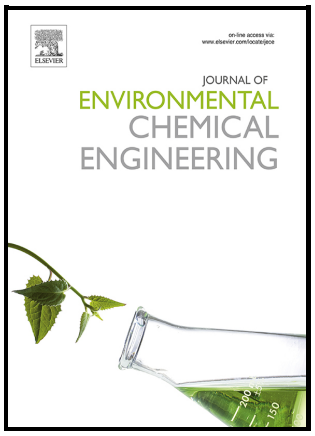

Impact of the duty cycle on the morphology and photocatalytic properties of S-TiO_2 obtained by plasma electrolytic oxidation to treat real electaroplating wastewater contaminated with Cr^{6+}

Steven Vargas-Villanueva, Juan Pablo Velásquez-Tamayo, Darwin Augusto Torres-Cerón, D. Fabio Mercado, Ricardo A. Torres-Palma, David Riassetto, Julieta Soledad Riva, S. Amaya-Roncancio, Samir Fernando Castilla-Acevedo, Elisabeth Restrepo-Parra

PII: S2213-3437(23)00985-5

DOI: https://doi.org/10.1016/j.jece.2023.110246

Reference: JECE110246

To appear in: *Journal of Environmental Chemical Engineering*

Received date: 2 February 2023
Revised date: 7 May 2023
Accepted date: 30 May 2023

Please cite this article as: Steven Vargas-Villanueva, Juan Pablo Velásquez-Tamayo, Darwin Augusto Torres-Cerón, D. Fabio Mercado, Ricardo A. Torres-Palma, David Riassetto, Julieta Soledad Riva, S. Amaya-Roncancio, Samir Fernando Castilla-Acevedo and Elisabeth Restrepo-Parra, Impact of the duty cycle on the morphology and photocatalytic properties of S-TiO_2 obtained by plasma electrolytic oxidation to treat real electaroplating wastewater contaminated with Cr^{6+}, *Journal of Environmental Chemical Engineering,* (2023) doi:https://doi.org/10.1016/j.jece.2023.110246

Impact of the duty cycle on the morphology and photocatalytic properties of S-TiO_2 obtained by plasma electrolytic oxidation to treat real electroplating wastewater contaminated with Cr^{6+}

Steven Vargas-Villanueva [1], Juan Pablo Velásquez-Tamayo [1], Darwin Augusto Torres-Cerón [*, 1, 2, 9], D. Fabio Mercado [*, 3, 4], Ricardo A. Torres-Palma [3], David Riassetto [4], Julieta Soledad Riva [5, 6], S. Amaya-Roncancio [*, 7, 8] Samir Fernando Castilla-Acevedo [8, 10], and Elisabeth Restrepo-Parra [1].

[1] Plasma Physics Laboratory, Universidad Nacional de Colombia Sede Manizales, Manizales, Colombia.
[2] Department of Mathematics, Universidad Tecnológica de Pereira (UTP), Pereira, Colombia
[3] Grupo de Investigación en Remediación Ambiental y Biocatálisis (GIRAB), Instituto de Química, Facultad de Ciencias Exactas y Naturales, Universidad de Antioquia UdeA, Calle 70 No. 52-21, Medellín, Colombia.
[4] Grenoble INP, LMGP, Institute of Engineering, Université Grenoble Alpes, 38000 Grenoble, France.
[5] Faculty of Mathematics Astronomy, Physics and Computer Studies, Universidad Nacional de Córdoba, Córdoba, Argentina.
[6] National Council for Scientific and Technical Research, CONICET (for its acronym in Spanish), Córdoba, Argentina.
[7] PCM Computational Applications, Universidad Nacional de Colombia Sede Manizales, Manizales, Colombia.
[8] Natural and Exact Sciences department, Universidad de la Costa, Barranquilla, Colombia.
[9] Gestión & Medio Ambiente, Manizales Caldas, Colombia.
[10] Chemical & Petroleum Engineering Department, The University of Kansas, Lawrence, KS 66047, United States.

*** Corresponding author:** dtorresce@unal.edu.co
*** Corresponding author:** d.fabiomercado@gmail.com
*** Corresponding author:** samaya3@cuc.edu.co

Abstract

This work reports S-TiO_2 doped coatings to reduce Cr^{6+} to Cr^{3+} obtained from a Ti electrode through the Plasma Electrolytic Oxidation (PEO) process. The Ti sheets (20 x 20 x 1 mm) were submerged on 0.1 M H_2SO_4, and values of the duty cycle from 2% to 50% were applied to obtain various materials. SEM, XRD, AFM, XPS, and DRS techniques were used to characterize the resultant surfaces. It was observed that the duty cycle strongly influences the

crystalline/amorphous ratio, anatase/rutile ratio, porosity density, pores size distribution, and surface roughness. Besides, it is explained that the introduction of SO_4^{2-} into the TiO_2 structure can take place either in the Ti or O places in the crystalline lattice. All materials showed photocatalytic properties to reduce Cr^{6+} to Cr^{3+} under UVC light (254 nm), decreasing the efficiency with the increase of the duty cycle. Additionally, the introduction of EDTA showed a positive synergy with the heterogeneous photocatalytic process when the material was obtained with the highest duty cycle. This last result was attributed to the relatively low bandgap and the high recombination rate; furthermore, EDTA acts as holes and hydroxyl radical scavenger. Thus, the photoelectrochemical system for the treatment of wastewater was evaluated, and again, the same materials showed the highest performance. In the same way, the re-use of the material obtained with the 2% duty cycle was tested, getting satisfactory results, obtaining 96.14±2.77% Cr^{6+} reduction even after seven cycles of reuse.

Keywords: Cr^{6+}, Reduction, PEO, Duty Cycle, wastewater, S-TiO_2.

1. Introduction

Chromium (Cr) is one of the most hazardous heavy metals causing environmental pollution nowadays, it is found in two different oxidation states: hexavalent (Cr^{6+}) and trivalent chromium (Cr^{3+}). Cr^{6+} is the most toxic state with high bioaccumulation and is used primarily in the leather and electroplating industry [1,2], while Cr^{3+} is the least toxic and it is necessary for the proper functioning of living beings [3]. Nevertheless, the oxidation of Cr^{3+} to Cr^{6+} has been reported to occur during the chlorination process in conventional wastewater treatment [4] and thus the removal of Cr from water is required. The World Health Organization

(WHO) has established a maximum limit of about 0.05 mg L^{-1} Cr presence in drinking water [5].

Chemical reduction, precipitation, flotation, electrolysis, electrocoagulation, and membrane-based techniques have been reported to treat water contaminated with Cr^{6+} [6–9]. However, the use of these technologies is limited due to the elevated costs for implementation or the production of secondary contaminants [10]. Adsorption stands out for its easy operation, relatively high performance, and economic feasibility in removing Cr [11,12]. The typical limitation of the process comes from the requirement of developing materials with high surface area, and the additional unit processes required to remove the solid-liquid mixture [13]. Thus, it is necessary to develop new alternatives for treating water contaminated with Cr^{6+}.

Heterogeneous photocatalysis is an alternative process, which has attracted scientific attention due to its capacity to promote the reduction of Cr^{6+} to Cr^{3+} with relatively low energy consumption [14,15]. Heterogenous photocatalysis uses semiconductor materials as photocatalyst, being Titanium dioxide (TiO_2) the most common due to its chemical stability and high photocatalytic activity [16]. TiO_2 has been extensively studied both theoretical and experimentally due to its optical and psychochemical properties and have shown interesting properties for both Cr^{6+} to Cr^{3+} reduction and posterior Cr^{3+} adsorption [17].

Several syntheses and coating methods have been used to obtain different functional TiO_2 materials, such as hydrothermal [18], sol-gel [19], chemical vapor deposition (CVD) [20], solvothermal [21] and magnetron sputtering [22]. However, the robust equipment required

or the weak coating adhesion to the substrate makes it difficult to use the obtained materials for real water treatment applications.

In recent years, Plasma Electrolytic Oxidation (PEO) has prompted great interest since it allows obtaining compact, rugged, dense, and well-adhered ceramic coatings on the surface of different metals such as titanium, magnesium, zinc, and their alloys [23,24]. Using PEO presents benefits over a simple electrolytic oxidation, such as more rigid and crystalline ceramic phases, high adhesion to the substrate under mechanical stress, and the possibility of porous growth on the oxide layer with chemical elements from the electrolyte solution.

The PEO technique is a low-cost and environmentally friendly technology. It is performed with a diluted electrolytic aqueous solution at high voltages, typically 200 V or higher, which develops a strong electric field that generates electric discharges on the substrate surface. This strong electric field establishes a plasma state that creates high local temperatures, between 2000 and 10,000 K. During the process, many micro discharge channels gradually grow up to reduce pressure when the current is increased, forming those plasma channels on the surface of the material [25] .

The parameters for synthesis in the PEO process are operation time [26], type and concentration of electrolyte [27,28], frequency, useful duty cycle, and current density [29]. Thus, selecting the electrolyte for the synthesis is a critical step [30]. Furthermore, coatings with different structures, compositions, and properties can be obtained depending on the substrate material, the chemical composition of the electrolyte, the oxidation time, and electrical parameters such as the frequency and the value of the applied voltage [27,31].

Moreover, the duty cycle (time when the power source is on during a cycle) affects the porosity, porous size, and roughness of the synthesized material [32,33]. Unfortunately, this critical parameter has not been thoroughly studied, and its role in the photocatalytic properties of the TiO_2 obtained is not well understood.

The aim of this study is to evaluate the impact of the duty cycle on the properties of the synthesized S-TiO_2 coatings on a Ti substrate using the PEO process when using H_2SO_4 as electrolyte. The synthesized materials were evaluated in the photoreduction of Cr^{6+} in real electroplating wastewater. In some cases, EDTA was introduced in the solution to evaluate its influence in the reduction. Finally, a photoelectrochemical approach was applied to overcome the performance limitation on the pure photochemical process. This study opens an interesting panorama for the design of versatile and reusable materials in the remediation of Cr^{6+}.

2. Materials and methods

2.1. Materials

Sulfuric acid (H_2SO_4, 96% wt. - PanReac AppliChem), phosphoric acid (H_3PO_4, 85% wt. – Sigma Aldrich), Ethylenediaminetetraacetic acid disodium salt dihydrate ($C_{10}H_{14}N_2Na_2O_8 \cdot 2H_2O$, 99% wt. – Loba Chemie), potassium dichromate ($K_2Cr_2O_7$, 99.5% wt. – Loba Chemie), 1,5-diphenylcarbazide ($C_{13}H_{14}N_4O$, 98% wt. - Loba Chemie) and acetone (C_3H_6O, 99.5% wt. - Loba Chemie) were used without further purification. Grade 2 Titanium sheets (99% wt. - ASTM B265 dimensions 20 x 20 x 1 mm from Electrónica I+D Ltda.) were used as substrates for the PEO process.

The Cr^{6+} photocatalytic reduction tests were performed using real plating wastewater. The physicochemical characterization of this water is shown in Table 1.

Table 1. Physicochemical characterization of electroplating wastewater.

Physicochemical parameters	Value
Cr (VI) (mg L^{-1})	13.25
Total Cr (mg L^{-1})	13.63
Cr (III) (mg L^{-1})	0.38
pH	5.89
Electric conductivity (µS cm^{-1})	90.65
Turbidity (NTU)	5.6
Total Ni (mg L^{-1})	0.78
Total organic carbon (mg L^{-1})	1.03
Inorganic carbon (µg mL^{-1})	362.5
Total Nitrogen (mg L^{-1})	2.20

2.2. PEO Coating process

A previous protocol developed by S. Vargas-Villanueva et al. was adapted to synthesize the S-TiO_2 doped sheets [30]. The Ti sheets were washed with water and then polished with SiC abrasive paper with a grit size of 320 – 1200. Subsequently, the polished Ti sheets were suspended in isopropanol and sonicated using a BUEHLER Ultramet 2002 Sonic clearer for 10 min. This process was repeated using distilled water as solvent. Then, the corresponding material was dried and washed three times with distilled water and dried at room temperature.

A switched source with a maximum output voltage of 357 V and frequency of 2000 Hz was used for the PEO process. A single sheet was submerged in 380 mL of an electrolyte solution of 0.1 M H_2SO_4, and different duty cycles were applied with values of 2, 10, 30, and 50% of the cycle time with a specified time of 500 µs. For all cases, the total time was

7 min (see Figure 1. **Schematic diagram of the assembly and process of the PEO system.**

An attempt was made to make a control sample of a TiO_2 coating without H_2SO_4 in the electrolyte. However, due to the low conductivity of the solution it was not possible to generate crystalline phases of anatase or rutile as observed in Figure S1. Therefore, it was not considered in this study as a control sample.

). Finally, all coatings were submerged in distilled water for two hours to remove traces of salt from the surface.

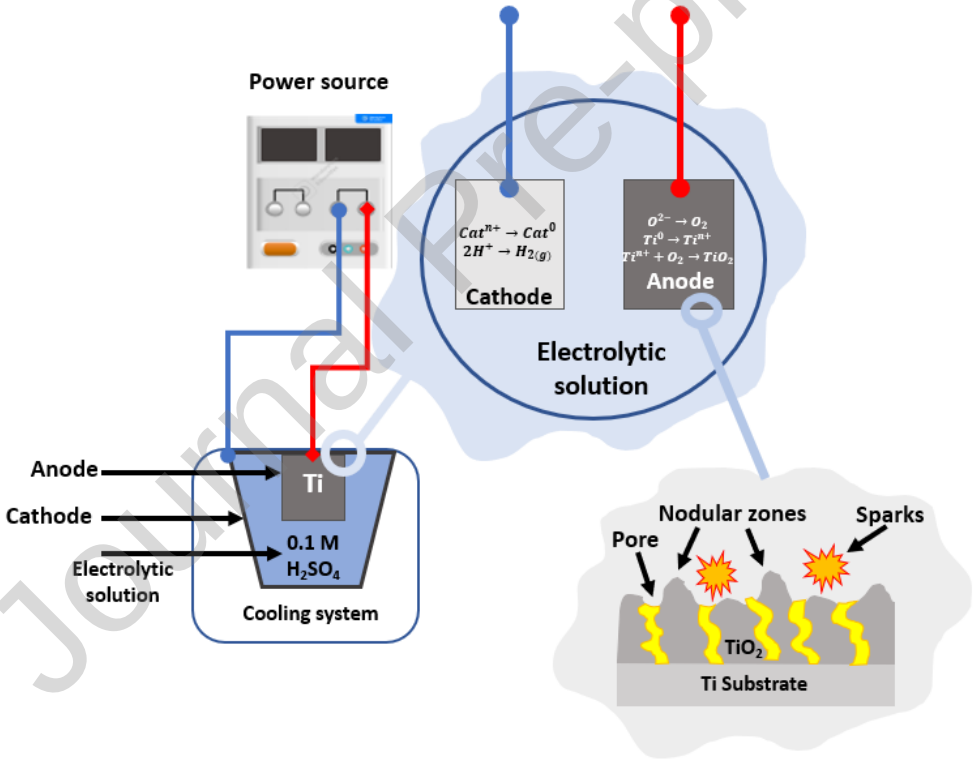

Figure 1. Schematic diagram of the assembly and process of the PEO system.

An attempt was made to make a control sample of a TiO_2 coating without H_2SO_4 in the electrolyte. However, due to the low conductivity of the solution it was not possible to generate crystalline phases of anatase or rutile as observed in Figure S1. Therefore, it was not considered in this study as a control sample.

2.3. Material characterization

X-Ray Diffraction (XRD) analyses were carried out in a Bruker Advance D8 X-Ray diffractometer with Bragg-Brentano geometry and a Cu source (λ = 1.541874 Å) at 40 kV and 40 mA. The estimation of the anatase/rutile ratio was carried out following the Spurr-Myers method [34]. Furthermore, the corresponding crystalline domains were quantified through the Williamsons Halls method [35]. The morphology of the coatings was obtained using a Carl Zeiss Field Emission Scanning Electron Microscope (FESEM) using electron and 5 kV irradiation with 10000× magnification and 20.0 µm aperture size. Atomic Force Microscopy (AFM) was used to analyze the topography and roughness of the surfaces. A HITACHI AFM5100N equipped with a 10 Å diameter Si_3N_4 tip was used in contact mode for a maximum area of 100 x 100 μm^2. Data processing was carried out using the free software Gwyddion v 2.50. The static contact angle measurement was performed on a 10 Mk2 Drop Shape Analysis (DSA) system provided by KRÜSS. For each measurement, 15 µL of distilled water pH 6.7 were placed on top of the corresponding surface. The baseline detection was carried out manually by the operator. X-ray photoelectron spectroscopy (XPS) spectra were obtained under a high ultra-vacuum with a K-alpha+ system (Thermo Fisher Scientific) using a gun type of Al K Alpha source with 400 µm spot size and CAE analyzer mode: Pass Energy 50.0 eV. Internal calibration to correct for the surface charge was performed with the C1s peak at BE = 284.8 eV due to adventitious carbon. High-resolution XPS spectra were further taken to analyze the chemical environment of the different elements. The analysis was carried out using the software Avantage®, and for all cases, a Shirley-type background of each spectrum was used. Besides, all the experimental curves were solved by Gaussian-Lorentzian fitting and compared with X-ray Photoelectron

Spectroscopy Database from NIST [36]. The bandgap values for each coating were obtained by UV–vis Diffuse Reflectance Spectra (DRS) using a Shimadzu Uv-2600 spectrophotometer with a wavelength range of 250 – 1000 nm.

2.4. Cr^{6+} photoreduction test.

The photocatalytic reduction of Cr^{6+} was carried out using real electroplating wastewater (See Table 1). In some cases, dilutions with Milli-Q water were prepared to obtain 4 or 1 mg Cr^{6+} L^{-1}, which is the common concentration found in electroplating wastewater in Colombia (see Figure S2). When required, 4 mg L^{-1} of EDTA were dissolved in the solution before the reaction in further experiments where the influence of this substance in the reduction of Cr^{6+} was evaluated. A typical photocatalytic experiment uses the setup shown in Figure S3 a. The experiment begins by turning on the lamp (OSRAM, 75W, $\lambda = 253 \pm 10$ nm) outside the setup and waiting 30 min to stabilize the photons emitted by the lamp. Subsequently, the selected material is immersed in 20 mL of reaction volume at pH 2.0 (adjusted by H_3PO_4). Finally, the lamp is positioned at 7.0 cm from the top of the recipient, and the reaction time starts counting. Samples of 0.8 mL were taken every 30 min and those were filtered using 0.23 µm cellulose syringe filters to be subsequently measured in an MRC UV-61PCS UV-Vis spectrophotometer at 540 nm. The measurement of the conversion of Cr^{6+} to Cr^{3+} was carried out using the Standard Methods 3500 Cr-B [37] by complexing the Cr^{6+} with 1.5-diphenylcarbazide following the protocol described in [38]. All the measurements were performed by triplicate and the average is reported along with its error bars.

A synergy effect (S) was calculated for cases in which EDTA was used to promote the photoreduction of Cr^{6+}. This synergy was obtained as the standardized difference between the photoreduction performance obtained where the material and EDTA (CPR_{comb}) were

simultaneously used as well as the sum of the performances obtained under either EDTA or materials individually (PR_i). The equation used to calculate the synergy is shown in Eq. 1 [39].

$$S = \frac{CPD_{comb} - \sum_1^n PR_i}{CPD_{comb}} \quad \text{(Eq. 1)}$$

2.5. Cr^{6+} Photo-electroreduction tests.

Photo-electroreduction tests were also carried out in a closed electric system where no electrical potential was applied. In this case, the synthesized material was connected to an untreated titanium sheet using Aluminum alligator clips attached to a copper cable of 2.05 mm diameter (see Figure S3 b). Later, both materials were immersed in the reactant solution, and the synthesized surface was irradiated using the same lamp used for the photocatalytic reduction tests.

3. Results and discussion

3.1. Material characterization

The X-ray diffractograms for the untreated Ti sheet and the treated ones by the PEO process at different duty cycles (DC) are shown in Figure 2. For the non-treated Ti-substrate (black line) the peaks at 34.9, 38.4, 40.1, 53.0, and 62.9° correspond to the planes (100), (002), (101), (102) and (110) of commercially pure Ti [40]. After the PEO treatment, all samples exhibit new diffraction bands. First, the signals at 25.4 and 48.1° correspond to the (101) and (200) planes of the TiO_2 anatase phase (JCPDS No. 21-1272). The peaks at 27.5, 36.2, 41.5, 44.2, 54.6, and 56.8° confirm the presence of the rutile phase (JCPDS No. 21–1276) [41].

The peak at 27.5° is attributed to the plane (110). The absence of a peak at around 30.8° indicates no Brookite phase in the resultant material synthesized [42,43].

These results suggest that the PEO treatment promotes first the reactive dissolution and posterior oxidation of the Ti substrate, producing anatase and rutile phases. However, the formation of amorphous phases should not be discarded.

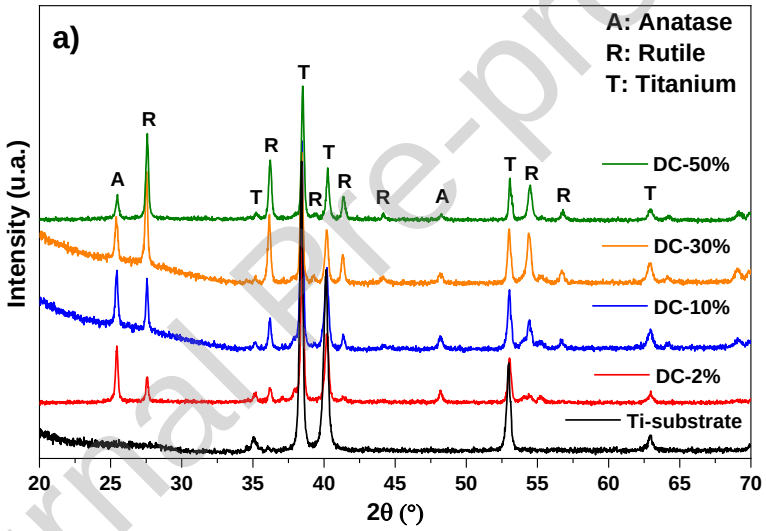

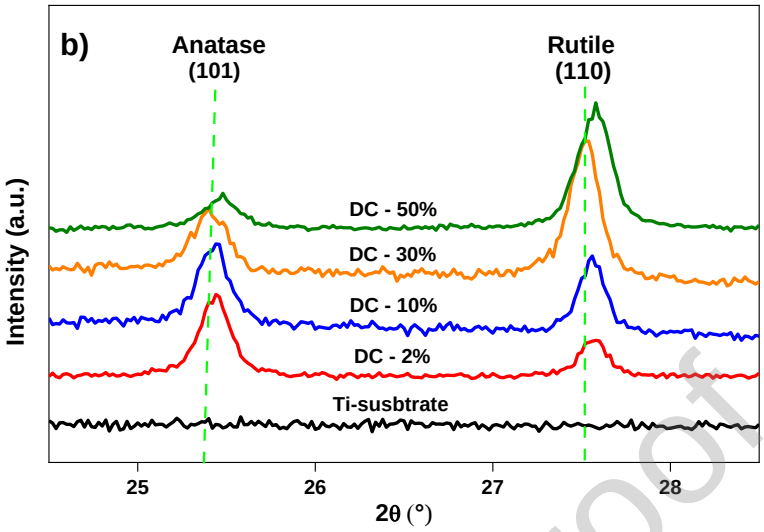

Figure 2. Vertically shifted XRD diffractograms. a) Ti-substrate samples, DC-2%, DC-10%, DC-30%, and DC-50%. b) selected magnified regions of the XRD diffractograms.

Figure 2b shows an inversion of the peak intensity in the phases (101) for anatase and (110) for rutile when the duty cycle (DC) increases. Figure S4 a shows the experimental anatase/rutile ratio are 1.75, 0.83, 0.32, and 0.20 for the samples at DC-2, DC-10, DC-30, and DC-50, respectively. All the previous results indicate an increase in selectivity for the rutile phase when the duty cycle is increased. The higher initial anatase fraction could be expected at the studied conditions since anatase is the first phase to crystallize due to its more flexible TiO_6 octahedron assembly sharing 4-edges under a kinetically control regime [44]. Subsequently, anatase could be transformed either in rutile or amorphous phases, but the conversion to an amorphous phase takes place at high energy duty cycles [44].

The results from numeric integrations on the X-ray diffractograms (plotted in Figure S4 b), show an increase in the sample crystalline fraction when increasing the duty cycle from 2 to 30% but the area of the diffractogram decreases by 29% when the duty cycle is increased up

to 50%. This result suggests that the amorphous phase increases at a duty cycle higher than 30%, supporting the previous statement about the transformation of anatase to amorphous phases [45]. Furthermore, the changes in the sizes of the crystalline domains for anatase and rutile, being possible to observe that the mean crystalline size remained statistically constant at 63 nm for anatase. For rutile, the crystalline size decreased from 262 to 51 nm. Hence, it is concluded that increasing the duty cycle also favors the formation of nanometric anatase and rutile phases [45]. The convergence of the crystal domain to 51 nm suggests that the domain frontiers do not suffer alterations occurring only in the phase transition from anatase to rutile.

Figure 2b also shows a change in the maximum peaks for lower and higher 2θ values in the samples at DC-30% and DC- 50%, suggesting an expansion and a contraction in the unit cell. Typically, these unit cell size changes indicate the introduction of heteroatoms in the crystalline structure. Thus, all the XPS spectra illustrated in Figure 3 were taken to understand this behavior. The survey XPS spectra shown in Figure 3a explain the presence of Ti, O, S, and C elements for all samples treated. Peak C is due to adventitious contamination, and this one was used to correct the binding energy to 284.8 eV due to charging effects. Omitting the C contribution, the surface stoichiometry for DC-2% and DC-50% are $Ti_{1.000}O_{1.325}S_{0.009}$ and $Ti_{1.000}O_{1.728}S_{0.015}$, respectively. This result suggests that increasing the duty cycle enhances both O and S surface concentration.

High-resolution XPS (HR-XPS) spectra were obtained for each one of the elements, and those are depicted in Figures 3b, 3c, and 3d. The $Ti2p^{3/2}$ and $Ti2p^{1/2}$ doublet were observed for Ti2p (Figure 3b) in the DC-50% samples. The maximum peaks were at 458.1 (for $Ti2p^{3/2}$)

and 463.8 eV (for $Ti2p^{1/2}$), and a satellite of 471.3 eV. These features align with the titanium standard binding energy in pure TiO_2, which supports the presence of Ti^{4+} [46]. The deconvolution of these two peaks suggests the presence of five different doublets that could be related to various chemical environments. The bands at 456.8 and 462.6 eV show the presence of surface Ti^{3+}, suggesting an incomplete surface oxidation or the in-situ production of Ti_2O_3 [47,48]. The second doublet (maximums at 459.2 and 465.3 eV) corresponds to Ti^{4+}, which is consistent with TiO_2 [49]. Interestingly, the doublet at 458.8 and 464.6 eV advises the Ti-O-S group, consistent with the XRD analysis of introducing heteroatoms in the unit cell [30]. The last bands at 459.2 and 465.3 eV could be attributed to oxygen vacancies in the surface layer [46].

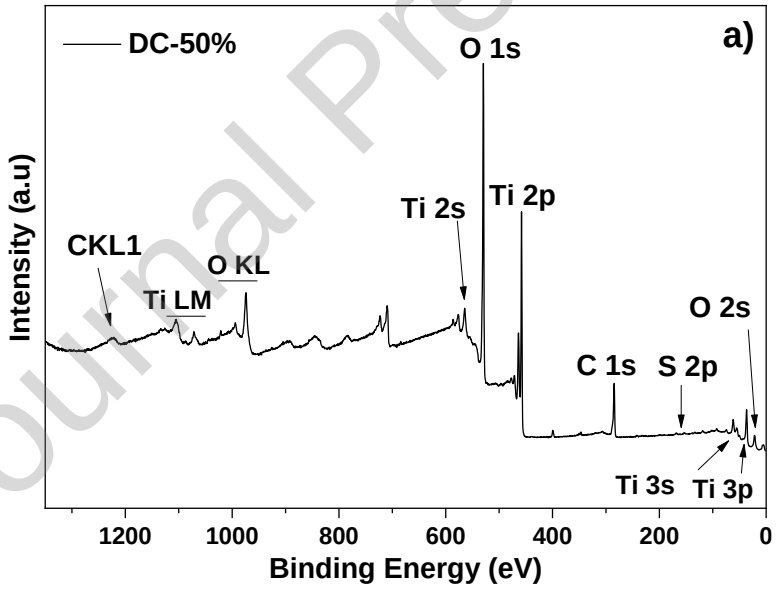

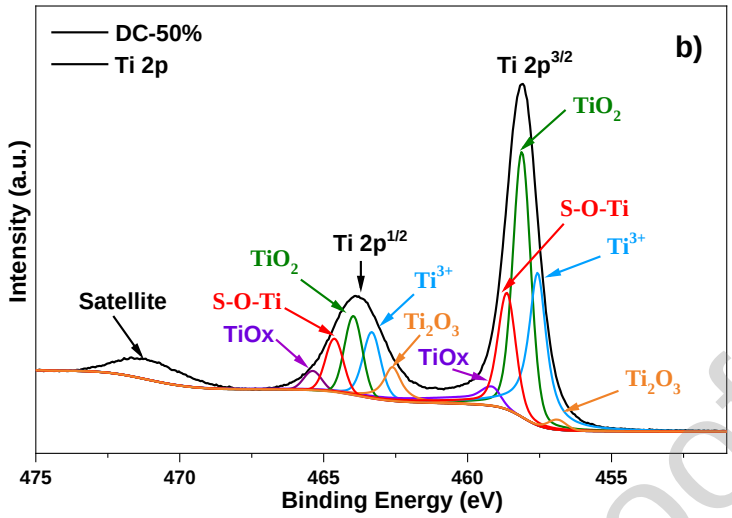

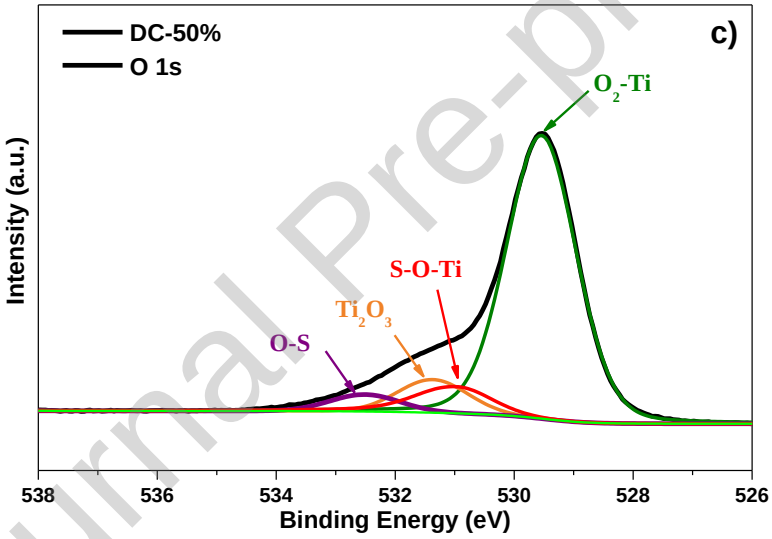

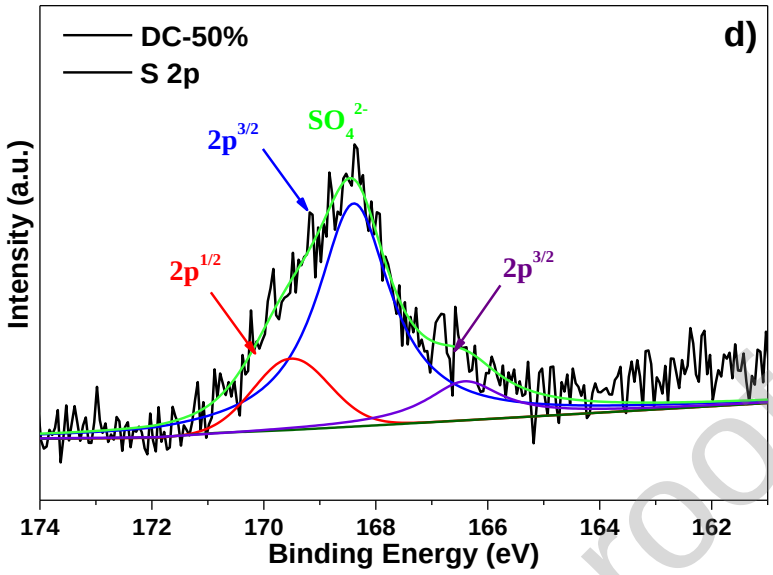

Figure 3. XPS spectra of the treated samples. a) survey spectra for DC-50%. b) Ti2p for DC-50%. c) O1s for DC-50%. d) S2p for DC-50%.

The O1s HR-XPS spectra in Figure 3c shows a maximum peak at 529.6 eV. Its deconvolution resulted in the elucidation of four different species. The first species is shown at a maximum of 529.6 eV attributed to the lattice oxygen belonging to the TiO_2 domains [46]. The second species is the Ti-O-S cluster represented by the band at 530.9 eV. The third species is Ti_2O_3, observed at 531.3 eV, and the last band at 532.5 eV shows the presence of O-H and O-S bonding. This band is attributed to adsorbed hydroxyl and sulfate or sulfite ions [50].

Figure 3d shows the signals corresponding to S2p, where a doublet with a maximum of 168.4 and 169.2 eV was observed [30,51]. This doublet corresponds to the $S2p^{3/2}$ and $S2p^{1/2}$ environments. Boningari et al. obtained similar XPS results of synthesized TiO_2 nanoparticles doped with S. They attributed the XPS result to the S^{6+} and S^{4+} species at the Ti positions in the TiO_2 structure [50]. In this case, SO_4^{2-} or HSO_4^- ions formed by the dissociation of H_2SO_4 can act as a Lewis base and can react with Ti^{4+} ions with Lewis acid

behavior. This reaction could produce $Ti(SO_4)^{2+}$ in the lattice with O^{2-} free surface clusters that could act as nucleation sites for further growth of the solid due to the high energy in the system. Then, the last results suggest the introduction of $-SO_4^{2-}$ and $-SO_3^{2-}$ ions in the TiO_2 structure. This analysis agrees with the unit cell contraction and expansion hypothesis from the observations of the XRD diffractograms for the samples. S can form substitutional solutions with TiO_2 since the atomic radius of S is very similar to the radius of Ti (1.00 Å vs. 1.47 Å, respectively) and not very distant from the radius of O (0.6 Å). Thus, A unit cell contraction can be observed when S atoms take Ti positions in the crystalline structure (as shown for the DC-50% sample) while an expansion is observed if S takes O positions in the structure (as shown for DC-30% sample). In fact, the signal between 163.2 – 164.2 eV [52] could be related to introducing S^{2-} species into the O^{2-} sites in the unit cell which is consistent with the previous statement [52]. These results are interesting since they show that the introduction of S into a Ti or O space might be related to the duty cycle used, although further investigation is needed [53].

The SEM micrographs in Figure 4 display the changes in topography due to the PEO process. Figure 4a show that the untreated Ti substrate exhibits a flat surface. Once the PEO treatment is carried out, the Ti substrates develop a pore-like structure even for the lowest duty cycle applied (DC-2%). Further analysis demonstrates that the pore size distribution is also affected by the duty cycle applied (Figure S5). The average pore diameters were 78.5, 91.3, 136.7, and 142.9 nm for the DC-2%, DC-10%, DC-30% and DC-50% samples, respectively. Moreover, the relative abundance of pores with a relatively high mean diameter (< 500 nm) also increases with the duty cycle.

Although the mechanism of metal oxide film formation assisted by the PEO treatment is still under discussion, some authors suggest that the spark discharge region could reach temperatures as high as 10000 K due to the Joule effect [54,55]. This Joule effect produces the melting of the substrate in the discharge channels accompanied by the development of pressures as high as 10^3 MPa [56]. In this regard, the reported melting temperature of Ti is 1941 K. Therefore, the pores observed in the micrographs of the treated samples could be due to the melting of the non-porous Ti substrate (see Figure 4a). Moreover, the increase in mean pore size with duty cycle could be due to the greater spread of the melted mass.

The experimental time window applied in this study was an active pulse of 10 µs, which corresponds to 10 times the reported by Yerokhin et al. as the period to develop and release temperature and pressure (less than 1 µs) [57]. Consequently, it is reasonable to expect that higher values than 1 µs will develop a porous structure, as this study shows, even for the lowest duty cycle applied.

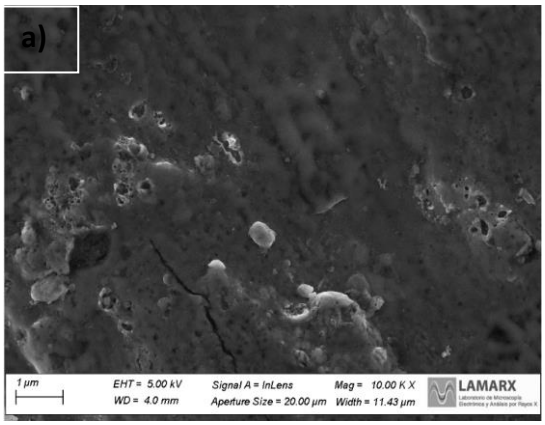
a)
1 µm
EHT = 5.00 kV
WD = 4.0 mm
Signal A = InLens
Aperture Size = 20.00 µm
Mag = 10.00 K X
Width = 11.43 µm
LAMARX

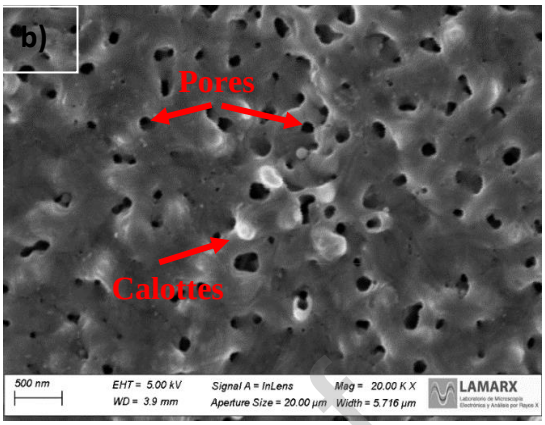
b)
Pores
Calottes
500 nm
EHT = 5.00 kV
WD = 3.9 mm
Signal A = InLens
Aperture Size = 20.00 µm
Mag = 20.00 K X
Width = 5.716 µm
LAMARX

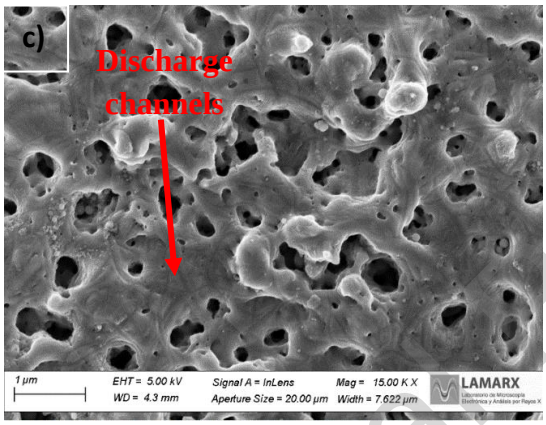
c)
Discharge channels
1 µm
EHT = 5.00 kV
WD = 4.3 mm
Signal A = InLens
Aperture Size = 20.00 µm
Mag = 15.00 K X
Width = 7.622 µm
LAMARX

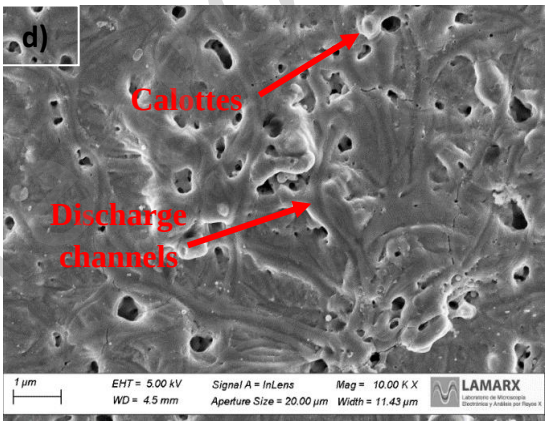
d)
Calottes
Discharge channels
1 µm
EHT = 5.00 kV
WD = 4.5 mm
Signal A = InLens
Aperture Size = 20.00 µm
Mag = 10.00 K X
Width = 11.43 µm
LAMARX

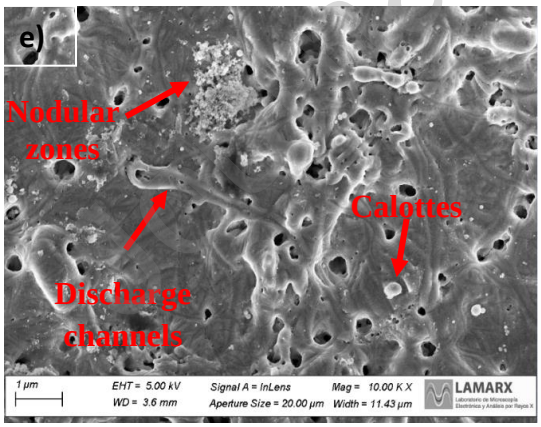
e)
Nodular zones
Calottes
Discharge channels
1 µm
EHT = 5.00 kV
WD = 3.6 mm
Signal A = InLens
Aperture Size = 20.00 µm
Mag = 10.00 K X
Width = 11.43 µm
LAMARX

Figure 4. Selected SEM micrographs of a) untreated Ti substrate, b) DC-2%, c) DC-10%, d) DC-30% and e) DC-50%. The words and arrows in red are intended to identify some structural features analyzed in the text.

Several reports state that the discharge mechanism is due to the dielectric breakdown of the surface which takes place in localized domains with lower electrical resistance [45][54]. The dielectric breakdown forms the so-called discharge channels characterized by convergence to the pores. These channels become more concentrated on the surface with an increasing duty cycle consistent with increasing roughness. These structures are evident in some of the micrographs. Figure S6 shows a more apparent micrograph to distinguish them on the surface. Calottes (spherical structures) can be also seen in Figure S6 and they have been previously reported in several studies [58].

When the melted Ti expelled from the newly formed pores interacts with the relatively cold solvent, it fuses to create a solid that could be adsorbed again on the electrode surface. This adsorption in the electrode increases the total width of the oxide/substrate. Therefore, surfaces with higher roughness are expected at higher temperatures, as well as increasing the duty cycles. Similarly, the melted substrate fraction can be high at higher duty cycles and the re-solidification process is not uniform. This results in the formation of non-uniform solids on the surface called nodular zones as evidenced by the SEM micrographs for the DC-50% sample.

Some AFM micrographs shown in Figure 5 and the contact angle (CA) measurements in Figure S7 agree with the results from the SEM analysis. Figure 5 shows that the experimental roughness increases with the increase of the duty cycle as follows: 133 ± 23, 173 ± 21, 218 ± 22, and 266 ± 20 nm for DC-2%, DC-10%, DC-30%, and DC-50%, respectively. In addition, Figure S7 shows an increase of CA from 97.7° to 115.3° from the untreated Ti substrate to the DC-50% sample. According to Wenzel, the roughness increase is proportional to the rise in the static contact angle of a surface [59].

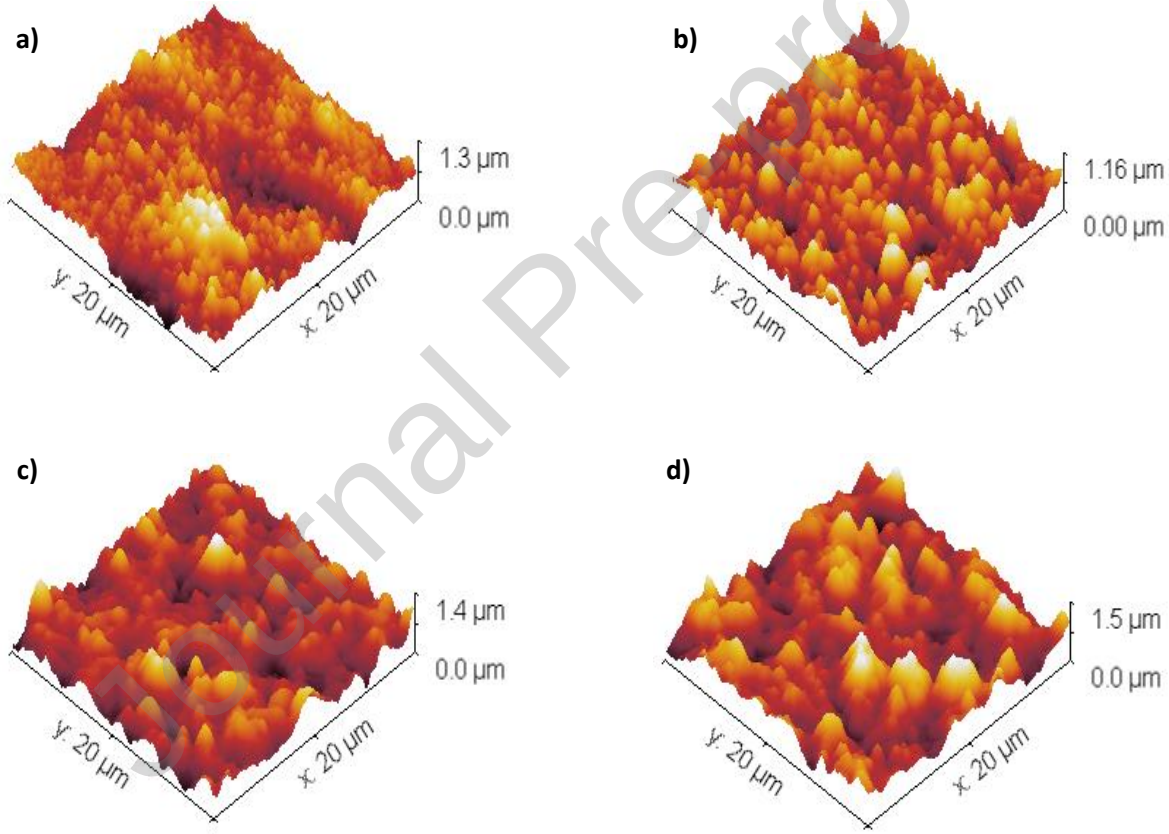

Figure 5. AFM micrographs. a) DC-2%. b) DC-10%. c) DC-30%. d) DC-50%.

Based on the previous results, the following formation mechanism is proposed. First, the reactive dissolution of the Ti-substrate (**Reaction 1**) [57] takes place due to the relatively high potential on the substrate and the discharge take place with the conductive surrounding

solution. Moreover, the formation of titanium dioxide takes place due to the reaction of the Ti^{4+} with the hydroxyl anion produced by the dissociation of water molecules (**Reaction 2**).

$$Ti^{0} \rightarrow Ti^{4+} + 4e^{-} \qquad \textbf{Reaction 1}$$

$$Ti^{4+} + 4HO^{-} \rightarrow TiO_{2(s)\downarrow} + 2H_2O + 4e^{-} \qquad \textbf{Reaction 2}$$

Moreover, due to the high energy onto the system, the ions SO_4^{2-} or HSO_4^{-} formed by the dissociation of the H_2SO_4, act as a Lewis base which can react with Ti^{4+} ions with Lewis acid behavior producing $Ti(SO_4)^{2-}$ like domains on the network with free O^{2-} surface groups that might act as nucleation sites for further growth of the solid.

The UV-Vis absorption spectra and their corresponding Tauc-plots are shown in Figure 6a and Figure 6b. Values of bandgaps are 2.87, 2.96, 2.76 and 2.05 eV for DC-10%, DC-2%, DC-30% and DC-50%, respectively. The latter results suggest that the PEO treatment not only impact on the surface composition and on the roughness but also on the optical properties of the obtained materials.

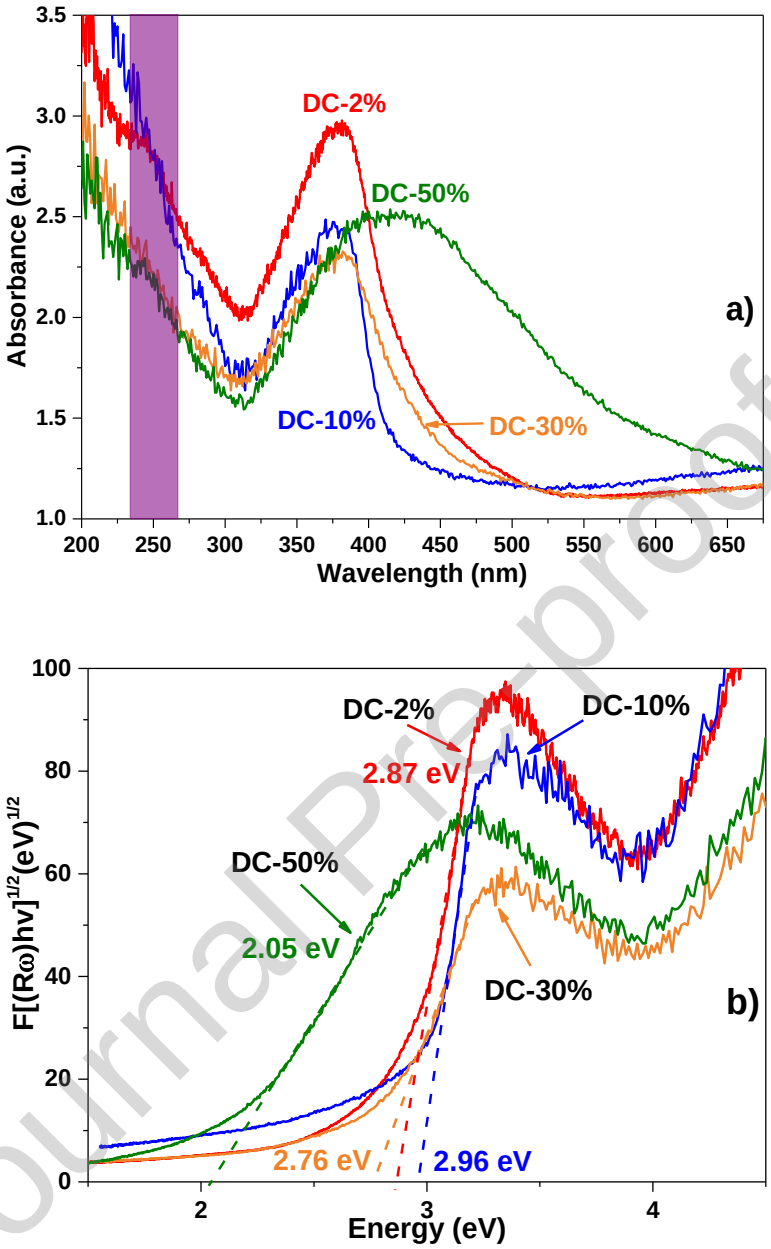

Figure 6. UV-Vis absorbance spectra and Tauc-plots for all treated samples. a) UV-Vis. b) Kubelka-Munk transformation to determine the bandgap.

3.2. Photocatalytic reduction of Cr^{6+}

All adsorption experiments were carried out using the real electroplating wastewater at pH 2.0, which contains the Cr^{6+}. For Cr concentration lower than 10 ppm and pH = 2.0, the main species are $Cr_2O_7^{2-}$ and $HCrO_4^-$ with almost equimolar concentrations [60]. Therefore, both species should be considered. In that regard, the reduction semi-reactions involved for them are shown in reactions 3 and 4 [61], with E° > 0 V, which confirms the spontaneity of the reaction with H^+ and electrons on the medium.

$$Cr_2O_7^{2-} + 14H^+ + 6e^- \rightarrow 2Cr^{3+} + 7H_2O \qquad E° = 1.33 \text{ V vs NHE} \qquad \textbf{Reaction 3}$$

$$HCrO_4^- + 7H^+ + 3e^- \rightarrow Cr^{3+} + 4H_2O \qquad E° = 1.35 \text{ V vs NHE} \qquad \textbf{Reaction 4}$$

An initial experiment was carried out by immersing the obtained materials in the wastewater without irradiation (dark conditions) for 120 minutes using the experimental setup shown in Figure S3 a. As observed in Figure 7a, the Cr^{6+} concentration removal (%) was less than 10% for all cases, equivalent to 0.1 mg L^{-1}. The low reduction performance of Cr^{6+} could be related to the weak reducing activity of TiO_2 in the ground state. Further experiments using irradiation with a photon source of $\lambda = 253 \pm 10$ nm (configuration shown in Figure S3 showed a more significant decrease in the Cr^{6+} concentration (Figure 7b). This higher performance in the reduction of Cr^{6+} cannot be attributed only to the action of light (black square in Figure 7b). Therefore, the results suggest that photocatalytic reduction from Cr^{6+} to Cr^{3+} took place. Moreover, the materials showed different performances for Cr^{6+} reduction, following the trend DC-50% < DC-30% < DC-10% < DC-2%.

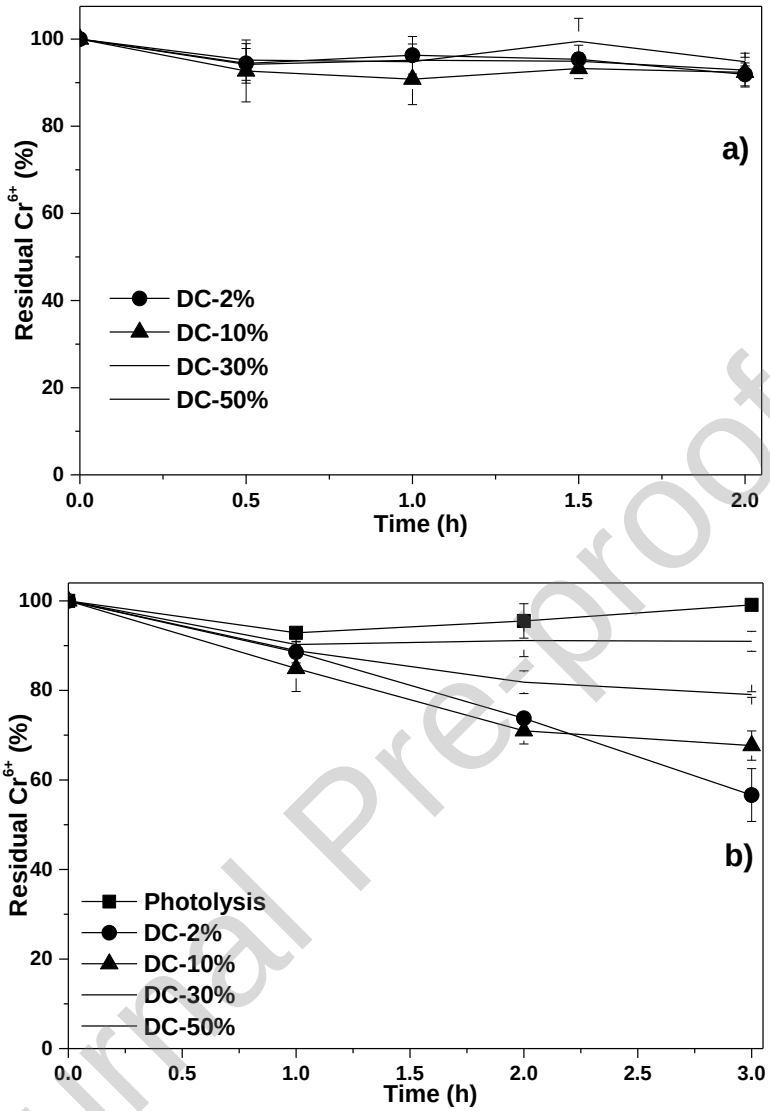

Figure 7. Cr^{6+} concentration profile for each material under different conditions. (a) darkness, (b) UV-C irradiation. For all cases the initial Cr^{6+} was 1 mg L^{-1} at pH 2.0.

As shown previously in Figure 6a, the DC-50% sample shows its maximum light absorption peak in the visible region, while the rest of the samples absorbs light in the UVA region. However, the shoulder highlighted in Figure 6a in the UV region (254 nm) results being higher for DC-2% and DC-10%, which is in agreement with the higher Cr^{6+} reduction performance. The modification of bandgaps in the treated samples could result in both a

kinetic and a thermodynamic change of the reactive process, making it difficult to understand the Cr^{6+} reduction performance differences observed in Figure 7. However, the DC-50% sample (lowest band gap of 2.05) could have the highest recombination, which could explain its lower performance.

The photoreduction of Cr^{6+} to Cr^{3+} mechanism mediated by TiO_2 has been widely explored [62,63]. TiO_2 in ground-state absorb a photon with the exact energy of the bandgap (Reaction 5) which promotes the migration of an electron from the valence band (V.B.) to the conduction band (C.B.) resulting on the formation of the electron-hole (e_{CB}^- - h_{VB}^+) pair. The produced photoelectron (e_{CB-}) might participate in the direct reduction of Cr^{6+} as following the chemical reactions previously mentioned (Reactions 3 and 4).

$$TiO_2 + h\upsilon \rightarrow h_{VB}^+ + e_{CB}^- \qquad \textbf{Reaction 5}$$

Additionally, the photoproduced e_{CB}^--h_{VB}^+ pair might react individually with the surrounding molecules. In fact, the photoholes (h_{VB}^+) could react with adsorbed water molecules to produce hydroxyl radical (HO·) as shown in Reaction 6. Regarding the e_{CB}^-, they might react with dissolved molecular oxygen producing a reaction cascade represented on **Reactions 7** – 11**,** which produces oxidation agents such as anion radical superoxide ($O_2{\cdot}^-$) [64], hydrogen peroxide (H_2O_2), and HO· [65]. Thus, reactions 7, 8 and 11 are competitive reactive pathways to the e_{CB}^--mediated Cr^{6+} photoreduction.

$$h_{VB}^+ + H_2O \rightarrow HO\cdot + H^+ \qquad \textbf{Reaction 6}$$

$$e_{CB}^- + O_2 \rightarrow O_2{\cdot}^- \qquad \textbf{Reaction 7}$$

$$e_{CB}^- + O_2 + H^+ \rightarrow HO_2\cdot \qquad \textbf{Reaction 8}$$

$$O_2{\cdot}^- + H_2O \rightarrow HO_2\cdot + HO^- \qquad \textbf{Reaction 9}$$

$$2HO_2\cdot \rightarrow O_2 + H_2O_2 \qquad \textbf{Reaction 10}$$

$$e_{CB}^- + H_2O_2 \rightarrow HO^- + HO\cdot \qquad \textbf{Reaction 11}$$

Therefore, the direct re-oxidation of Cr^{3+} through electron transfer to the h_{VB}^+ or due to its reaction with the hydroxyl radical HO· (E° = 2.80 V vs NHE) is also plausible [65].

The later analysis evidenced the complexity of the involved reactive pathway for the Cr^{6+} photoreduction. Furthermore, the mentioned discussion did not consider the impact on the different optical properties of the materials as the one used on this study (See **Figure 6**). The modification on the band gaps might result on both kinetic and thermodynamic modification of the reactive process, which complicates the understanding on the yield differences observed on Figure 4b. Nevertheless, the material DC-50%, which has the lowest band gap might be the one with the highest recombination yield of all the materials.

3.3. Influence of the addition of EDTA in the photocatalytic reduction of Cr^{6+}

The introduction of holes scavenger organic molecules and oxidizing species scavengers (such as EDTA) is an interesting approach to favor the photoreduction of Cr^{6+} over other competing reactions such as Cr^{3+} re-oxidation and to avoid the(e_{CB}^--h_{VB}^+) pair recombination. The photoreduction of Cr^{6+} was carried out in the presence of EDTA in solution. The results of these experiments are shown in Figure 8a. For the system without material (EDTA + UVC light), the introduction of EDTA resulted in a decrease of around 50% of the Cr^{6+} concentration. The last result suggests that EDTA plays an important role in the photoreduction of Cr^{6+}. Blank experiments in the absence of light suggest that EDTA itself does not promote the reduction of Cr^{6+} to Cr^{3+}, which is coherent with the literature [66]. Besides, due to the anionic nature of both Cr^{6+} species (*vide supra*) and the anionic nature of

EDTA (pKa = 2.0, 2.7, 6.2, and 10.3), at pH = 2.0, the formation of metal-organic complexes does not take place [67]. Thus, a possible route for the role of EDTA is as follows: EDTA acts as a h_{VB}^{+} scavenger, which avoids the (e_{CB}^{-}-h_{VB}^{+}) pair recombination and thus favoring the kinetic of the Cr^{6+} photoreduction. Furthermore, it might also avoid the Cr^{3+} reoxidation due to its reaction with either h_{VB}^{+} or HO·. For the latter case, HO· is known to have a non-selective behavior and thus the introduction of the EDTA might result on the decrease on the Cr^{3+} re-oxidation [66].

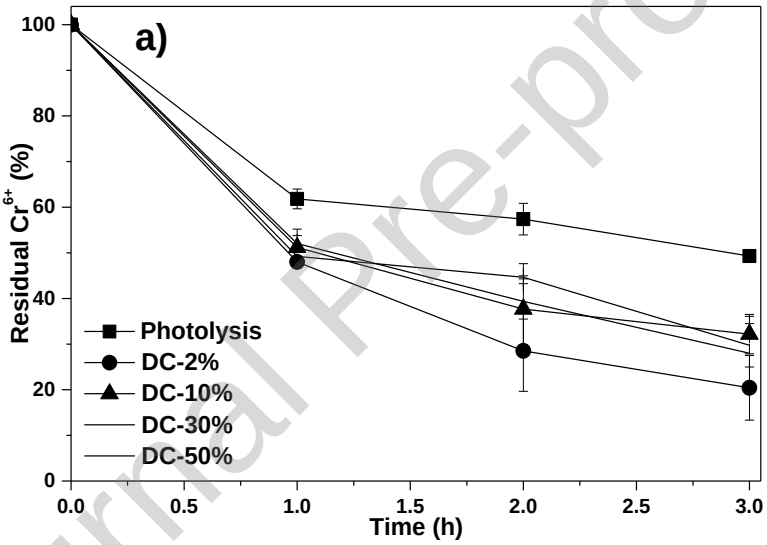

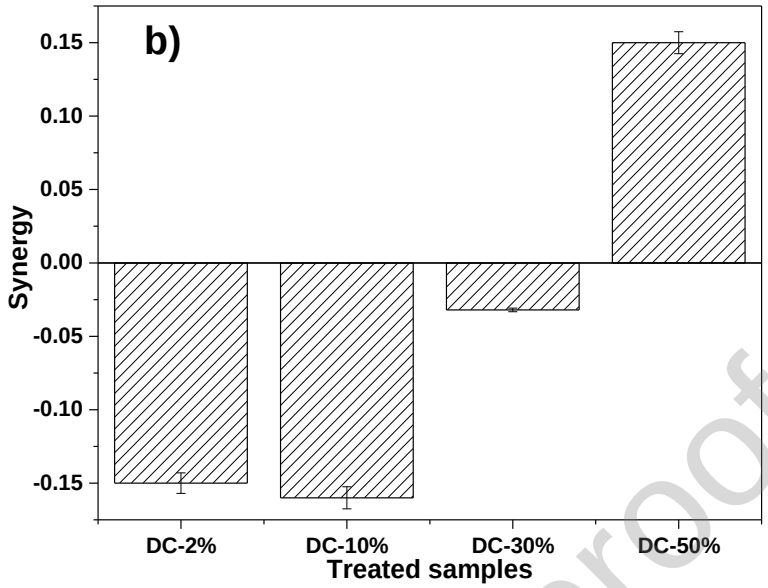

Figure 8. Cr^{6+} concentration profile for each material under different conditions. (a) photocatalytic reduction in the presence of 4 mg L^{-1} of EDTA. b) synergy. For all cases the initial Cr^{6+} was 1 mg L^{-1} at pH 2.0.

It is also observed in Figure 8a that the reduction of Cr^{6+} is higher for all the tests in the presence of EDTA (Figure 7a vs Figure 6b). Figure 8b shows the synergy between material-based and EDTA-based treatments for Cr^{6+} photoreduction process. Only the DC-50% material showed positive synergy suggesting that the final performance on the combined process is greater than the sum of the performance of the individual processes. For the EDTA-free system of this material (Figure 8b) a decrease performance of ~10% of Cr^{6+} was observed after three hours. For the system containing only EDTA and light, ~50% of Cr^{6+} was achieved. However, for the combination of both processes a removal of ~70% of Cr^{6+} was obtained. For all other cases, the performance observed for the material-EDTA system was lower than the obtained by the sum of the performance of individual EDTA and its corresponding material.

Regarding the latest results, the introduction of EDTA favors the performance of the DC-50% material in the reduction of Cr^{6+} to Cr^{3+} which is the one with the lowest bandgap and thus it might be the one with the highest (e_{CB}^--h_{VB}^+) pair recombination.

The scheme presented in Figure 9 shows the general pathway for the reduction of Cr^{6+} to Cr^{3+} in the absence and presence of EDTA.

a)

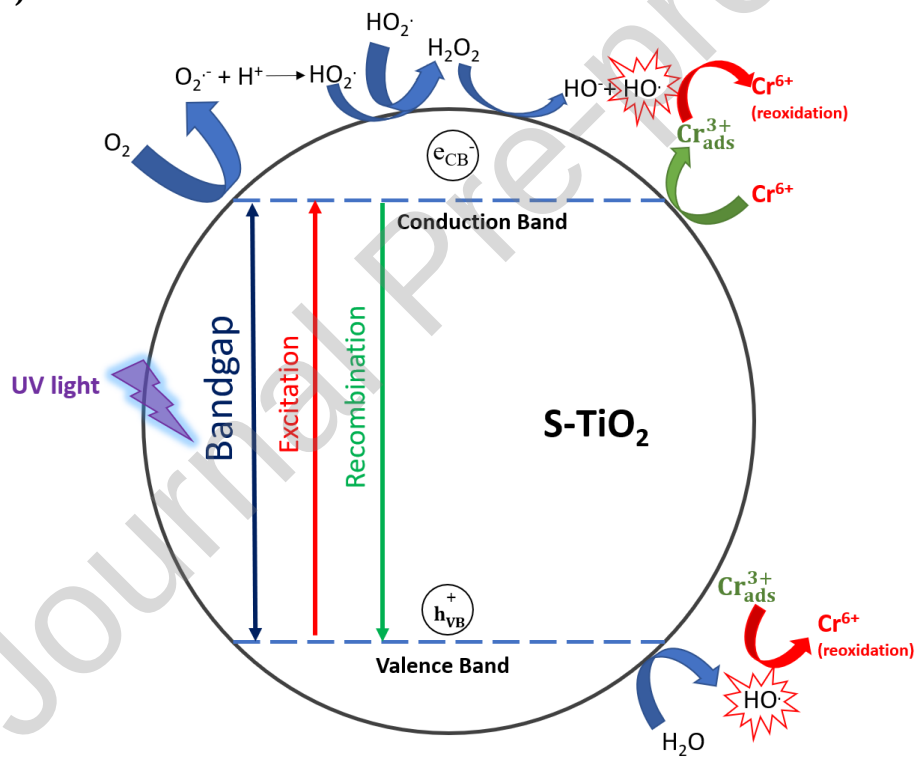

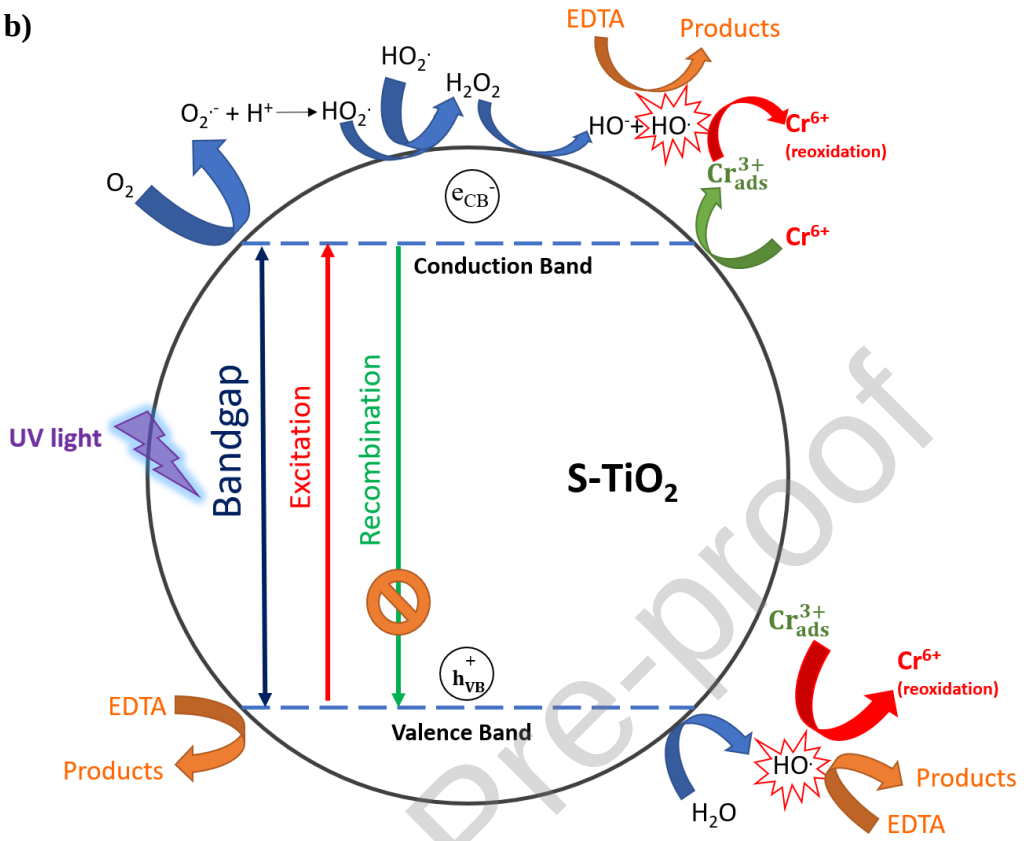

Figure 9. Possible reaction pathway for the reduction of Cr^{6+} to Cr^{3+} in the (a) absence and (b) presence of EDTA.

3.4. Photo-electroreduction of Cr^{6+}.

Electron-hole recombination affects the kinetic performance of the TiO_2-based photocatalytic process. Therefore, the diffusion of the e^-_{CB} away from the S-TiO_2 doped catalyst is an exciting approach to explore. For this reason, the existing photocatalyst was tested in an electrochemical cell connected with an additional Ti-substrate as a counter-electrode to close the circuit and only the S-TiO_2 material was irradiated (as shown in Figure S3 b). The behavior of the Cr^{6+} concentration is shown in Figure 10.

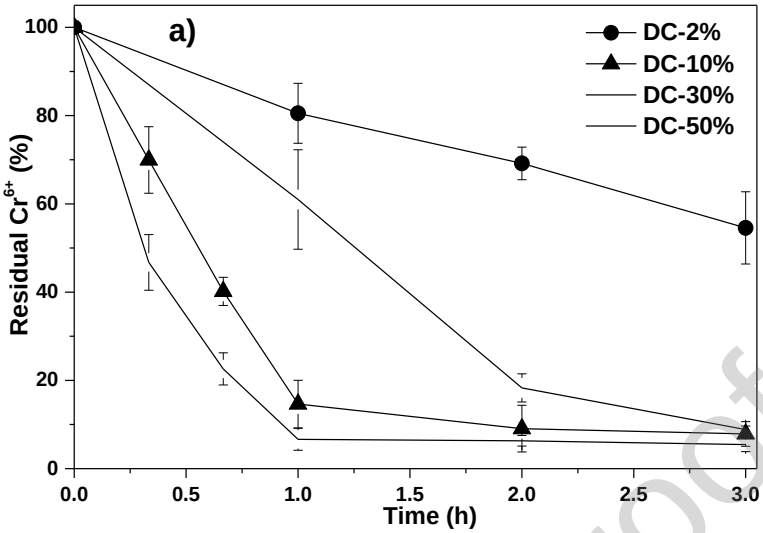

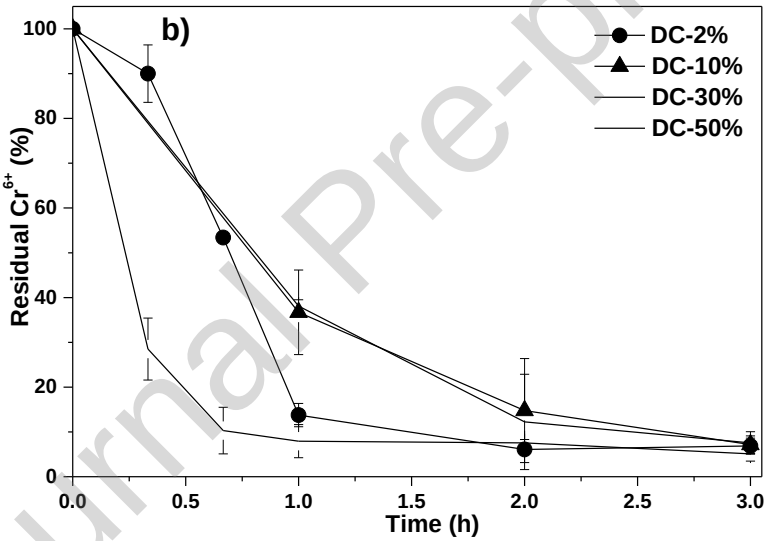

Figure 10. Cr^{6+} concentration profile for each material in the photoelectrochemical circuit under different conditions. a) irradiation without the presence of EDTA. b) irradiation with the presence of 4 mg L^{-1} EDTA. c) photograph showing the decrease in concentration of Cr^{6+} through the photocatalytic process. For all cases the initial Cr^{6+} was 1 mg L^{-1} at pH 2.0.

As shown in Figure 10a, the DC-50% sample (lowest bandgap) is the one that shows the rapidest depletion of Cr^{6+}. As mentioned previously, a low bandgap might promote a fast recombination rate. But closing the circuit promotes the diffusion of e^-_{CB} to the Ti electrode facilitating the separation of charges in the photocatalyst. Besides, an improvement in the photo-electro reduction system (Figure 10a) is observed compared to the photocatalytic reduction system for DC-10% and DC-30%. DC-10% is the second fastest material in this new setting, and it has the highest bandgap.

Furthermore, DC-50% and DC-2% samples are the fastest materials after the introduction of the EDTA (Figure 8c). For DC-50% in a closed circuit, the time to reach equilibrium at the lowest concentration of Cr^{6+} is 2 hours in the presence of EDTA but the equilibrium is not reached in the presence or absence of EDTA with the circuit open. Thus, it is concluded that after closing the circuit, the DC-50% material considerably improves its performance from 65% Cr^{6+} removal at 3 h (open circuit - in the presence of EDTA) to 90% in 1 h (closed circuit - in the presence of EDTA).

3.5. Photocatalyst reuse tests to reduce Cr^{6+}

Finally, the DC-2% materials were reused in several cycles to evaluate their reuse as shown in Figure 11 (a-b) and the material maintained its photoelectrochemical activity through 7 cycles of 25 mL of 4 mg L^{-1} Cr^{6+} real wastewater. These materials can be reused without loss of effectiveness thus, avoiding unitary operations for the separation of powder catalysis.

Considering that the interest in wastewater treatment for the reduction of Cr^{6+} through coatings obtained by the PEO process is growing and the difference in parameters of the PEO process is wide, the information found in the literature is limited. From the results obtained, these agree with the reported by Yao et al. [68] and Torres-Ceron et al. [69], in which they made TiO_2 coatings using the PEO process, and in the evaluation of the material they used $K_2Cr_2O_7$ (synthetic water).

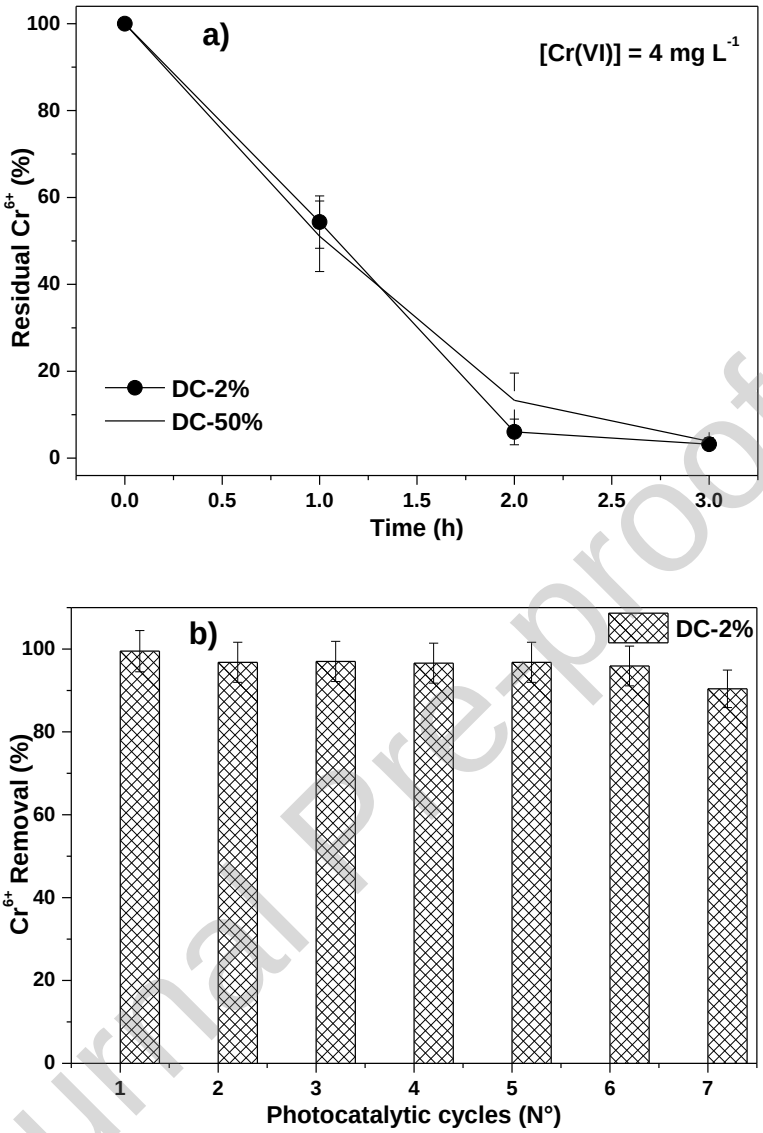

Figure 11. Cr^{6+} Concentration profile for each material on the photoelectrochemical circuit. (a) irradiation in the presence of 4 mg L^{-1} EDTA for DC-2% and DC-50%. (b) cycles use for the DC-2% sample. For all cases the initial Cr^{6+} was 4 mg L^{-1} at pH 2.0.

4. Conclusions

Several S-doped TiO_2 coatings were obtained on a Ti electrode by the PEO process. It was observed that the duty cycle impacts the crystalline/amorphous ratio but also the

anatase/rutile ratio. Along the same lines, the duty cycle impacts on the porosity density but also on the distribution size of the surface pores and the surface roughness. It is clarified that the introduction of SO_4 ions into the TiO_2 structure takes place at places originally of Ti in the crystal lattice.

The bandgap of the obtained material depended on the duty cycle used. But more importantly, the material obtained at 50% duty cycle developed a relatively low band of 2.05 eV. However, although all the materials showed photocatalytic properties regarding Cr^{6+} reduction and subsequent adsorption from a real galvanized wastewater, the mentioned material showed the lowest performance. Nevertheless, after the introduction of EDTA, the system containing the same material showed the highest synergy between the individual processes. Therefore, it is clarified that the DC-50% material has a relative high electron-hole recombination rate. Thus, the photoelectrochemical processes overcome the high electron-hole rate of recombination of this material and hence it was the fastest to photo-reduce Cr^{6+} to Cr^{3+} with subsequent Cr^{3+} adsorption. In addition, it showed high reusability.

5. Acknowledgments

The authors thank Universidad Nacional de Colombia, Manizales Campus for the financial support of Minciencias within the framework of the program "*Implementación de un sistema de tratamiento para aguas residuales provenientes de la industria del cromado*", and Universidad Nacional de Colombia, Manizales Campus for the financial support of the "*Implementación de tecnologías limpias para el tratamiento de superficies para el sector de la galvanotecnia, con énfasis en la gestión de residuos y eficiencia hídrica y ambiental para*

la industria en Caldas, Código BPIN: 2021000100388". S.F. Castilla-Acevedo thanks M.F. Guzman-Acosta for all the support and useful discussions.

6. References

[1] M. Brumovský, J. Oborná, P. Lacina, M. Hegedüs, O. Sracek, J. Kolařík, M. Petr, J. Kašlík, T. Hofmann, J. Filip, Sulfidated nano-scale zerovalent iron is able to effectively reduce in situ hexavalent chromium in a contaminated aquifer, J Hazard Mater. 405 (2021) 124665. https://doi.org/10.1016/J.JHAZMAT.2020.124665.

[2] I. Ali, J.O. Kim, Visible-light-assisted photocatalytic activity of bismuth-TiO_2 nanotube composites for chromium reduction and dye degradation, Chemosphere. 207 (2018) 285–292. https://doi.org/10.1016/J.CHEMOSPHERE.2018.05.075.

[3] J. Zhou, Y. Wang, J. Wang, W. Qiao, D. Long, L. Ling, Effective removal of hexavalent chromium from aqueous solutions by adsorption on mesoporous carbon microspheres, J Colloid Interface Sci. 462 (2016) 200–207. https://doi.org/10.1016/J.JCIS.2015.10.001.

[4] D.R. Lindsay, K.J. Farley, R.F. Carbonaro, Oxidation of CrIII to CrVI during chlorination of drinking water, Journal of Environmental Monitoring. 14 (2012) 1789. https://doi.org/10.1039/c2em00012a.

[5] World Health Organization, Guidelines for Drinking water Quality 3 ed, Geneva, 2004.

[6] H. Qi, S. Wang, H. Liu, Y. Gao, T. Wang, Y. Huang, Synthesis of an organic–inorganic polypyrrole/titanium(IV) biphosphate hybrid for Cr(VI) removal, J Mol Liq. 215 (2016) 402–409. https://doi.org/10.1016/J.MOLLIQ.2015.12.060.

[7] P. Malaviya, A. Singh, Physicochemical Technologies for Remediation of Chromium-Containing Waters and Wastewaters, Crit Rev Environ Sci Technol. 41 (2011) 1111–1172. https://doi.org/10.1080/10643380903392817.

[8] R. Labied, O. Benturki, A.Y. Eddine Hamitouche, A. Donnot, Adsorption of hexavalent chromium by activated carbon obtained from a waste lignocellulosic material (Ziziphus jujuba cores): Kinetic, equilibrium, and thermodynamic study, Adsorption Science & Technology. 36 (2018) 1066–1099. https://doi.org/10.1177/0263617417750739.

[9] K.E. Ukhurebor, U.O. Aigbe, R.B. Onyancha, W. Nwankwo, O.A. Osibote, H.K. Paumo, O.M. Ama, C.O. Adetunji, I.U. Siloko, Effect of hexavalent chromium on the environment and removal techniques: A review, J Environ Manage. 280 (2021) 111809. https://doi.org/10.1016/j.jenvman.2020.111809.

[10] J. Saien, A. Azizi, A.R. Soleymani, Parameter evaluation, kinetics, and energy consumption for Cr(VI) photocatalytic reduction under mild conditions, Journal of the Iranian Chemical Society 2014 11:5. 11 (2014) 1439–1448. https://doi.org/10.1007/S13738-014-0419-5.

[11] W. Liu, L. Yang, S. Xu, Y. Chen, B. Liu, Z. Li, C. Jiang, Efficient removal of hexavalent chromium from water by an adsorption–reduction mechanism with sandwiched nanocomposites, RSC Adv. 8 (2018) 15087–15093. https://doi.org/10.1039/C8RA01805G.

[12] V.E. Pakade, N.T. Tavengwa, L.M. Madikizela, Recent advances in hexavalent chromium removal from aqueous solutions by adsorptive methods, RSC Adv. 9 (2019) 26142–26164. https://doi.org/10.1039/C9RA05188K.

[13] G.L. Dotto, G. McKay, Current scenario and challenges in adsorption for water treatment, J Environ Chem Eng. 8 (2020) 103988. https://doi.org/10.1016/j.jece.2020.103988.

[14] O.A. Arotiba, B.O. Orimolade, B.A. Koiki, Visible light–driven photoelectrocatalytic semiconductor heterojunction anodes for water treatment applications, Curr Opin Electrochem. 22 (2020) 25–34. https://doi.org/10.1016/j.coelec.2020.03.018.

[15] F. Di Natale, A. Erto, A. Lancia, D. Musmarra, Equilibrium and dynamic study on hexavalent chromium adsorption onto activated carbon, J Hazard Mater. 281 (2015) 47–55. https://doi.org/10.1016/J.JHAZMAT.2014.07.072.

[16] J.B. Islam, M. Furukawa, I. Tateishi, S. Kawakami, H. Katsumata, S. Kaneco, Enhanced photocatalytic reduction of toxic Cr(VI) with Cu modified ZnO nanoparticles in presence of EDTA under UV illumination, SN Appl Sci. 1 (2019) 1240. https://doi.org/10.1007/s42452-019-1282-x.

[17] C.M. Ma, Y.S. Shen, P.H. Lin, Photoreduction of Cr(VI) Ions in Aqueous Solutions by UV/ Photocatalytic Processes, International Journal of Photoenergy. 2012 (2012) 1–7. https://doi.org/10.1155/2012/381971.

[18] X. Jin, X. Zhou, P. Sun, S. Lin, W. Cao, Z. Li, W. Liu, Photocatalytic degradation of norfloxacin using N-doped TiO_2: Optimization, mechanism, identification of intermediates and toxicity evaluation, Chemosphere. 237 (2019) 124433. https://doi.org/10.1016/J.CHEMOSPHERE.2019.124433.

[19] M.P.B. Vega, M. Hinojosa-Reyes, A. Hernández-Ramírez, J.L.G. Mar, V. Rodríguez-González, L. Hinojosa-Reyes, Visible light photocatalytic activity of sol–gel Ni-doped TiO_2 on p-arsanilic acid degradation, Journal of Sol-Gel Science and Technology 2018 85:3. 85 (2018) 723–731. https://doi.org/10.1007/S10971-018-4579-0.

[20] J. Lang, K. Takahashi, M. Kubo, M. Shimada, Preparation of TiO_2-CNT-Ag Ternary Composite Film with Enhanced Photocatalytic Activity via Plasma-Enhanced Chemical Vapor Deposition, Catalysts 2022, Vol. 12, Page 508. 12 (2022) 508. https://doi.org/10.3390/CATAL12050508.

[21] R. Guo, Y. Bao, Q. Kang, C. Liu, W. Zhang, Q. Zhu, Solvent-controlled synthesis and photocatalytic activity of hollow TiO_2 microspheres prepared by the solvothermal method, Colloids Surf A Physicochem Eng Asp. 633 (2022) 127931. https://doi.org/10.1016/J.COLSURFA.2021.127931.

[22] L. Zhang, J. Guo, B. Hao, H. Ma, WO_3/TiO_2 heterojunction photocatalyst prepared by reactive magnetron sputtering for Rhodamine B dye degradation, Opt Mater (Amst). 133 (2022) 113035. https://doi.org/10.1016/J.OPTMAT.2022.113035.

[23] A.L. Yerokhin, X. Nie, A. Leyland, A. Matthews, Characterisation of oxide films produced by plasma electrolytic oxidation of a Ti–6Al–4V alloy, Surf Coat Technol. 130 (2000) 195–206. https://doi.org/10.1016/S0257-8972(00)00719-2.

[24] F. Simchen, M. Sieber, A. Kopp, T. Lampke, Introduction to Plasma Electrolytic Oxidation—An Overview of the Process and Applications, Coatings 2020, Vol. 10, Page 628. 10 (2020) 628. https://doi.org/10.3390/COATINGS10070628.

[25] S. Durdu, Ö.F. Deniz, I. Kutbay, M. Usta, Characterization and formation of hydroxyapatite on Ti6Al4V coated by plasma electrolytic oxidation, J Alloys Compd. 551 (2013) 422–429. https://doi.org/10.1016/J.JALLCOM.2012.11.024.

[26] O.A. Galvis, D. Quintero, J.G. Castaño, H. Liu, G.E. Thompson, P. Skeldon, F. Echeverría, Formation of grooved and porous coatings on titanium by plasma electrolytic oxidation in H_2SO_4/H_3PO_4 electrolytes and effects of coating morphology on adhesive bonding, Surf Coat Technol. 269 (2015) 238–249. https://doi.org/10.1016/j.surfcoat.2015.02.036.

[27] X. Lu, M. Mohedano, C. Blawert, E. Matykina, R. Arrabal, K.U. Kainer, M.L. Zheludkevich, Plasma electrolytic oxidation coatings with particle additions – A review, Surf Coat Technol. 307 (2016) 1165–1182. https://doi.org/10.1016/j.surfcoat.2016.08.055.

[28] A. Fattah-Alhosseini, M.K. Keshavarz, M. Molaei, S.O. Gashti, Plasma Electrolytic Oxidation (PEO) Process on Commercially Pure Ti Surface: Effects of Electrolyte on the Microstructure and Corrosion Behavior of Coatings, Metallurgical and Materials Transactions A 2018 49:10. 49 (2018) 4966–4979. https://doi.org/10.1007/S11661-018-4824-8.

[29] M. V Diamanti, M.P. Pedeferri, Effect of anodic oxidation parameters on the titanium oxides formation, 49 (2007) 939–948. https://doi.org/10.1016/j.corsci.2006.04.002.

[30] S. Vargas-Villanueva, D.A. Torres-Ceron, S. Amaya-Roncancio, I.D. Arellano-Ramírez, J.S. Riva, E. Restrepo-Parra, Study of the incorporation of S in TiO_2/SO_4^{2-} Coatings produced by PEO process through XPS and DFT, Appl Surf Sci. 599 (2022) 153811. https://doi.org/10.1016/j.apsusc.2022.153811.

[31] A.L. Yerokhin, X. Nie, A. Leyland, A. Matthews, S.J. Dowey, Plasma electrolysis for surface engineering, Surf Coat Technol. 122 (1999) 73–93. https://doi.org/10.1016/S0257-8972(99)00441-7.

[32] H. Khanmohammadi, S.R. Allahkaram, N. Towhidi, Microstructural, corrosion and mechanical behavior of two step plasma electrolyte oxidation ceramic coatings, Transactions of Nonferrous Metals Society of China. 27 (2017) 2225–2233. https://doi.org/10.1016/S1003-6326(17)60248-6.

[33] B. Yoo, K.R. Shin, D.Y. Hwang, D.H. Lee, D.H. Shin, Effect of surface roughness on leakage current and corrosion resistance of oxide layer on AZ91 Mg alloy prepared by plasma electrolytic oxidation, Appl Surf Sci. 256 (2010) 6667–6672. https://doi.org/10.1016/J.APSUSC.2010.04.067.

[34] R.A. Spurr, H. Myers, Quantitative Analysis of Anatase-Rutile Mixtures with an X-Ray Diffractometer, Anal Chem. 29 (1957) 760–762. https://doi.org/https://doi.org/10.1021/ac60125a006.

[35] J. Pelleg, E. Elish, D. Mogilyanski, Evaluation of average domain size and microstrain in a silicide film by the Williamson-Hall method, Metallurgical and Materials Transactions A. 36 (2005) 3187–3194. https://doi.org/10.1007/s11661-005-0089-0.

[36] V. Alexander, A. Naumkin, Kraut-Vass, W. Stephen, Gaarenstroom., J.P. Cedric, NIST X-ray Photoelectron Spectroscopy Database, Measurement Services Division of the National Institute of Standards and Technology (NIST). 20899 (2012) 20899. https://doi.org/10.18434/T4T88K.

[37] American Public Health Association (APHA), American Water Works Association (AWWA), Water Environment Federation (WEF), Standard Methods for the Examination of Water and Wastewater, 2017.

[38] A.V. Rangel, M.G. Becerra, H. Guerrero-Amaya, L.M. Ballesteros, D.F. Mercado, Sulfate radical anion activated agro-industrial residues for Cr(VI) adsorption: is this activation process technically and economically feasible?, J Clean Prod. 289 (2021) 125793. https://doi.org/10.1016/j.jclepro.2021.125793.

[39] R. Dewil, D. Mantzavinos, I. Poulios, M.A. Rodrigo, New perspectives for Advanced Oxidation Processes, J Environ Manage. 195 (2017) 93–99. https://doi.org/10.1016/j.jenvman.2017.04.010.

[40] M.-K. Han, J.-B. Im, M.-J. Hwang, B.-J. Kim, H.-Y. Kim, Y.-J. Park, Effect of Indium Content on the Microstructure, Mechanical Properties and Corrosion Behavior of Titanium Alloys, Metals (Basel). 5 (2015) 850–862. https://doi.org/10.3390/met5020850.

[41] L. Liu, H. Zhao, J.M. Andino, Y. Li, Photocatalytic CO_2 Reduction with H_2O on TiO_2 Nanocrystals: Comparison of Anatase, Rutile, and Brookite Polymorphs and Exploration of Surface Chemistry, ACS Catal. 2 (2012) 1817–1828. https://doi.org/10.1021/cs300273q.

[42] F. Scarpelli, T.F. Mastropietro, T. Poerio, N. Godbert, Mesoporous TiO_2 Thin Films: State of the Art, in: Titanium Dioxide - Material for a Sustainable Environment, InTech, 2018. https://doi.org/10.5772/intechopen.74244.

[43] M.T. Colomer, K.J. Duarte, A.L. Ortiz, D.F. Mercado, L.M. Ballesteros-Rueda, Influence of Pr^{3+} doping on the synthesis of colloidal sols and nanoparticulate TiO_2 xerogels and their photocatalytic activity, Mater Charact. 182 (2021) 111536. https://doi.org/10.1016/j.matchar.2021.111536.

[44] M. Gonçalves, J. Pereira, J. Matos, H. Vasconcelos, Photonic Band Gap and Bactericide Performance of Amorphous Sol-Gel Titania: An Alternative to Crystalline TiO_2, Molecules. 23 (2018) 1677. https://doi.org/10.3390/molecules23071677.

[45] D.A. Torres-Ceron, E. Restrepo-Parra, C.D. Acosta-Medina, D. Escobar-Rincon, R. Ospina-Ospina, Study of duty cycle influence on the band gap energy of TiO_2/P coatings obtained by PEO process, Surf Coat Technol. 375 (2019) 221–228. https://doi.org/10.1016/j.surfcoat.2019.06.021.

[46] H.-P. Qi, H.-L. Wang, Facile synthesis of Pr-doped molecularly imprinted TiO_2 mesocrystals with high preferential photocatalytic degradation performance, Appl Surf Sci. 511 (2020) 145607. https://doi.org/10.1016/j.apsusc.2020.145607.

[47] K. Yang, Y. Dai, B. Huang, Understanding Photocatalytic Activity of S- and P-Doped TiO_2 under Visible Light from First-Principles, Journal of Physical Chemistry C. 111 (2007) 18985–18994. https://doi.org/10.1021/JP0756350.

[48] D.A. Torres-Ceron, S. Amaya-Roncancio, J.S. Riva, A. Vargas-Eudor, D. Escobar-Rincon, E. Restrepo-Parra, Incorporation of P^{5+} and P^{3-} from phosphate precursor in TiO_2:P coatings produced by PEO: XPS and DFT study, Surf Coat Technol. 421 (2021) 127437. https://doi.org/10.1016/j.surfcoat.2021.127437.

[49] M. Murata, K. Wakino, S. Ikeda, X-ray photoelectron spectroscopic study of perovskite titanates and related compounds: An example of the effect of polarization on chemical shifts, J Electron Spectros Relat Phenomena. 6 (1975) 459–464. https://doi.org/10.1016/0368-2048(75)80032-6.

[50] T. Boningari, S.N.R. Inturi, M. Suidan, P.G. Smirniotis, Novel one-step synthesis of sulfur doped-TiO_2 by flame spray pyrolysis for visible light photocatalytic degradation of acetaldehyde, Chemical Engineering Journal. 339 (2018) 249–258. https://doi.org/10.1016/j.cej.2018.01.063.

[51] T. Dickinson, A.F. Povey, P.M.A. Sherwood, Dissolution and passivation of nickel. An X-ray photoelectron spectroscopic study, Journal of the Chemical Society, Faraday Transactions 1: Physical Chemistry in Condensed Phases. 73 (1977) 327–343. https://doi.org/10.1039/F19777300327.

[52] H. Martinez, C. Auriel, D. Gonbeau, M. Loudet, G. Pfister-Guillouzo, Studies of 1T TiS_2 by STM, AFM and XPS: the mechanism of hydrolysis in air, Appl Surf Sci. 93 (1996) 231–235. https://doi.org/10.1016/0169-4332(95)00339-8.

[53] M.R. Bayati, A.Z. Moshfegh, F. Golestani-Fard, Micro-arc oxidized S-TiO_2 nanoporous layers: Cationic or anionic doping?, Mater Lett. 64 (2010) 2215–2218. https://doi.org/10.1016/j.matlet.2010.07.010.

[54] M. Aliofkhazraei, D.D. Macdonald, E. Matykina, E.V. Parfenov, V.S. Egorkin, J.A. Curran, S.C. Troughton, S.L. Sinebryukhov, S.V. Gnedenkov, T. Lampke, F. Simchen, H.F. Nabavi, Review of plasma electrolytic oxidation of titanium substrates: Mechanism, properties, applications and limitations, Applied Surface Science Advances. 5 (2021) 100121. https://doi.org/10.1016/j.apsadv.2021.100121.

[55] J. Cai, F. Cao, L. Chang, J. Zheng, J. Zhang, C. Cao, The preparation and corrosion behaviors of MAO coating on AZ91D with rare earth conversion precursor film, Appl Surf Sci. 257 (2011) 3804–3811. https://doi.org/10.1016/J.APSUSC.2010.11.153.

[56] M.R. Bayati, F. Golestani-Fard, A.Z. Moshfegh, R. Molaei, In situ derivation of sulfur activated TiO_2 nano porous layers through pulse-micro arc oxidation technology, Mater Res Bull. 46 (2011) 1642–1647. https://doi.org/10.1016/j.materresbull.2011.06.017.

[57] A.L. Yerokhin, X. Nie, A. Leyland, A. Matthews, S.J. Dowey, Plasma electrolysis for surface engineering, Surf Coat Technol. 122 (1999) 73–93. https://doi.org/10.1016/S0257-8972(99)00441-7.

[58] B. Kasalica, M. Petković-Benazzouz, M. Sarvan, I. Belča, B. Maksimović, B. Misailović, Z. Popović, Mechanisms of plasma electrolytic oxidation of aluminum at the multi-hour

timescales, Surf Coat Technol. 390 (2020) 125681. https://doi.org/10.1016/J.SURFCOAT.2020.125681.

[59] R.N. Wenzel, Resistance of solid surfaces to wetting by water, Ind Eng Chem. 28 (1936) 988–994. https://doi.org/10.1021/ie50320a024.

[60] M. Szabó, J. Kalmár, T. Ditrói, G. Bellér, G. Lente, N. Simic, I. Fábián, Equilibria and kinetics of chromium(VI) speciation in aqueous solution – A comprehensive study from pH 2 to 11, Inorganica Chim Acta. 472 (2018) 295–301. https://doi.org/10.1016/J.ICA.2017.05.038.

[61] F.E.B. Coelho, V.M. Candelario, E.M.R. Araújo, T.L.S. Miranda, G. Magnacca, Photocatalytic Reduction of Cr(VI) in the Presence of Humic Acid Using Immobilized Ce–ZrO_2 under Visible Light, Nanomaterials 2020, Vol. 10, Page 779. 10 (2020) 779. https://doi.org/10.3390/NANO10040779.

[62] S.A. Rosli, N. Alias, N. Bashirom, S. Ismail, W.K. Tan, G. Kawamura, A. Matsuda, Z. Lockman, Hexavalent Chromium Removal via Photoreduction by Sunlight on Titanium–Dioxide Nanotubes Formed by Anodization with a Fluorinated Glycerol–Water Electrolyte, Catalysts 2021, Vol. 11, Page 376. 11 (2021) 376. https://doi.org/10.3390/CATAL11030376.

[63] J.B. Islam, M. Furukawa, I. Tateishi, H. Katsumata, S. Kaneco, Photocatalytic Reduction of Hexavalent Chromium with Nanosized TiO_2 in Presence of Formic Acid, ChemEngineering 2019, Vol. 3, Page 33. 3 (2019) 33. https://doi.org/10.3390/CHEMENGINEERING3020033.

[64] L. Xu, Y. Liu, Z. Hu, J.C. Yu, Converting cellulose waste into a high-efficiency photocatalyst for Cr(VI) reduction via molecular oxygen activation, Appl Catal B. 295 (2021) 120253. https://doi.org/10.1016/J.APCATB.2021.120253.

[65] M.I. Litter, Last advances on TiO_2-photocatalytic removal of chromium, uranium and arsenic, Curr Opin Green Sustain Chem. 6 (2017) 150–158. https://doi.org/10.1016/J.COGSC.2017.04.002.

[66] S. El Hakim, T. Chave, S.I. Nikitenko, Photocatalytic and sonocatalytic degradation of EDTA and Rhodamine B over Ti^0 and Ti@TiO_2 nanoparticles, Catalysts. 11 (2021) 928. https://doi.org/10.3390/CATAL11080928/S1.

[67] J. Threeprom, S. Purachaka, L. Potipan, Simultaneous determination of Cr(III)–EDTA and Cr(VI) by ion interaction chromatography using a C18 column, J Chromatogr A. 1073 (2005) 291–295. https://doi.org/10.1016/j.chroma.2004.09.053.

[68] Z. Yao, F. Jia, Y. Jiang, C. Li, Z. Jiang, X. Bai, Photocatalytic reduction of potassium chromate by Zn-doped TiO_2/Ti film catalyst, Appl Surf Sci. 256 (2010) 1793–1797. https://doi.org/10.1016/j.apsusc.2009.10.005.

[69] D.A. Torres, F. Gordillo-Delgado, J. Plazas-Saldaña, Formation of TiO_2 nanostructure by plasma electrolytic oxidation for Cr(VI) reduction, J Phys Conf Ser. 786 (2017) 012046. https://doi.org/10.1088/1742-6596/786/1/012046.

Graphical abstract

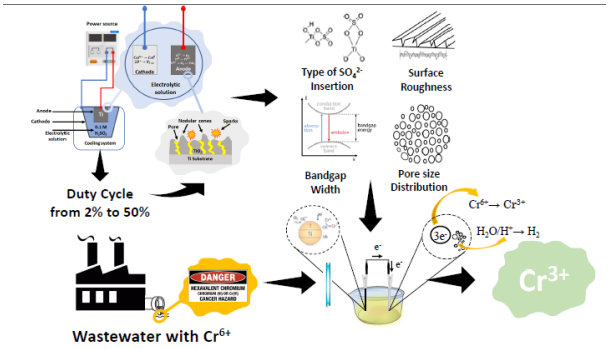

Credit author statement

D. A. Torres-Ceron: XPS data analysis, writing - original draft, review & editing.

S Vargas-Villanueva: writing - original draft, coatings production by PEO process and photocatalysis.

S. Amaya-Roncancio: Analysis and writing - original draft.

J.P. Velasquez-Tamayo: Coatings production by PEO process and photocatalysis.

D.F. Mercado: coating characterization, data analysis and review & editing.

J. Riva-Soledad: XPS measurements and XPS data analysis, data analysis.

E. Restrepo-Parra: review & editing, writing - original draft.

R. Torres-Palma: review & editing, writing - original draft.

D. Riassetto: coating characterization, writing and data curation.

S. F. Castilla-Acevedo: writing and data curation and review & editing.

Declaration of interests

☒ The authors declare that they have no known competing financial interests or personal relationships that could have appeared to influence the work reported in this paper.

☐The authors declare the following financial interests/personal relationships which may be considered as potential competing interests:

Highlights

- Duty cycle impacts on surface properties of roughness and pore size.
- Duty cycle impact the anatase/rutile composition and amorphous/crystalline ratio
- The band gap of the obtained material depended on the used duty cycle.
- Heavy duty reduction of Cr^{6+} to Cr^{3+} in raw wastewater probes.
- Under UV light all materials showed photocatalytic properties for Cr^{6+} reduction.